Sensitivity Analysis of Earthquake Depths in the Culberson–Mentone Earthquake Zone, Delaware Basin

Emmanuel Castillo*[1], Nadine Ushakov[1], and Alexandros Savvaidis[2]

Abstract

During the past decade, Texas has seen an increase in earthquakes linked to oil and gas operations. Although typically moderate in magnitude, their increasing frequency highlights the need to better understand induced seismicity. Accurate earthquake depth estimation is essential for understanding the physical mechanisms of induced seismicity but remains challenging in regions like the Culberson–Mentone earthquake zone (CMEZ) in the Delaware basin (DB), where earthquake depths are sparse and between 6 and 10 km below sea level. The challenges in this region include limited velocity models and complex and laterally heterogeneous geology. We introduce the *S-P* high-resolution catalog for CMEZ, refining TexNet depths using a two-step approach: *S-P* time differences and a local velocity model derived from sonic logs for events close to stations, and a relative relocation method for the remaining events. The results show consistent depths, revealing a deepening trend from west to east tied to the basement structure. Furthermore, the results suggest that deep seismicity in the CMEZ is controlled primarily by pore pressure diffusion from deep wastewater disposal injection zones, and it could be further influenced by earthquake-to-earthquake interactions that may facilitate stress transfer and fault reactivation at greater depths. These findings underscore the importance of dense seismic networks, accurate velocity models, and *S-P* times for accurate depth refinement, and highlight how continuous depth monitoring can improve understanding of induced seismicity and inform seismic hazard assessments in the DB.

Cite this article as Castillo, E., N. Ushakov, and A. Savvaidis (2026). Sensitivity Analysis of Earthquake Depths in the Culberson–Mentone Earthquake Zone, Delaware Basin, *Seismol. Res. Lett.* **XX**, 1–13, doi: 10.1785/0220250288.

Supplemental Material

Introduction

The Delaware basin (DB) is the western section of the Permian basin, one of the world's largest and most productive oil and gas provinces (U.S. Energy Information Administration, 2024). It extends across southeastern New Mexico and western Texas, United States (Fig. 1a). The region supports three main types of oil and gas operations: (1) conventional extraction, which relies primarily on vertical wells (Fig. 1b); (2) hydraulic fracturing (HF), which involves horizontal drilling to enhance hydrocarbon recovery from low-permeability formations (Fig. 1c); and (3) salt wastewater disposal (SWD), where produced water is injected into shallow and deep reservoirs with sufficient porosity to store large volumes of flowback water generated by both conventional and unconventional operations (Fig. 1d). These operations occur at varying depths and target different geological formations (Fig. 1e), and although they contribute significantly to energy production, they have also been associated with an increase in induced seismicity, highlighting the complex relationship between subsurface injection practices and geological stability in the basin.

For the past 50 yr, conventional vertical production has occurred primarily in the Delaware Mountain Group (DMG) and Bone Spring Group (Dvory and Zoback, 2021), which date to the Middle (Guadalupian) and Early Permian (Leonardian) ages, respectively. However, conventional drilling has significantly decreased over the last decade, whereas unconventional drilling has seen substantial growth, with more than 20,000 horizontal wells targeting the Wolfcamp Group, an unconventional reservoir from the Early Permian (Wolfcampian) age.

SWD operations involve both shallow and deep injection, each targeting different formations, depths, and volumes. Shallow injection, which handles the highest overall volume of wastewater, targets the DMG formation at depths ranging from 450 to 2400 m from the surface (Lemons *et al.*, 2019; Smye *et al.*, 2021, 2024; Ge *et al.*, 2022). In contrast, deep injection targets older, deeper carbonate formations from the Late

1. Department of Sustainable Earth Systems Sciences, The University of Texas at Dallas, Richardson, Texas, U.S.A., https://orcid.org/0000-0002-9799-9775 (EC); https://orcid.org/0000-0003-4093-7853 (NU); 2. Bureau of Economic Geology, Jackson School of Geosciences, The University of Texas at Austin, Austin, Texas, U.S.A., https://orcid.org/0000-0001-6373-5256 (AS)

*Corresponding author: emmanuel.castillotaborda@utdallas.edu

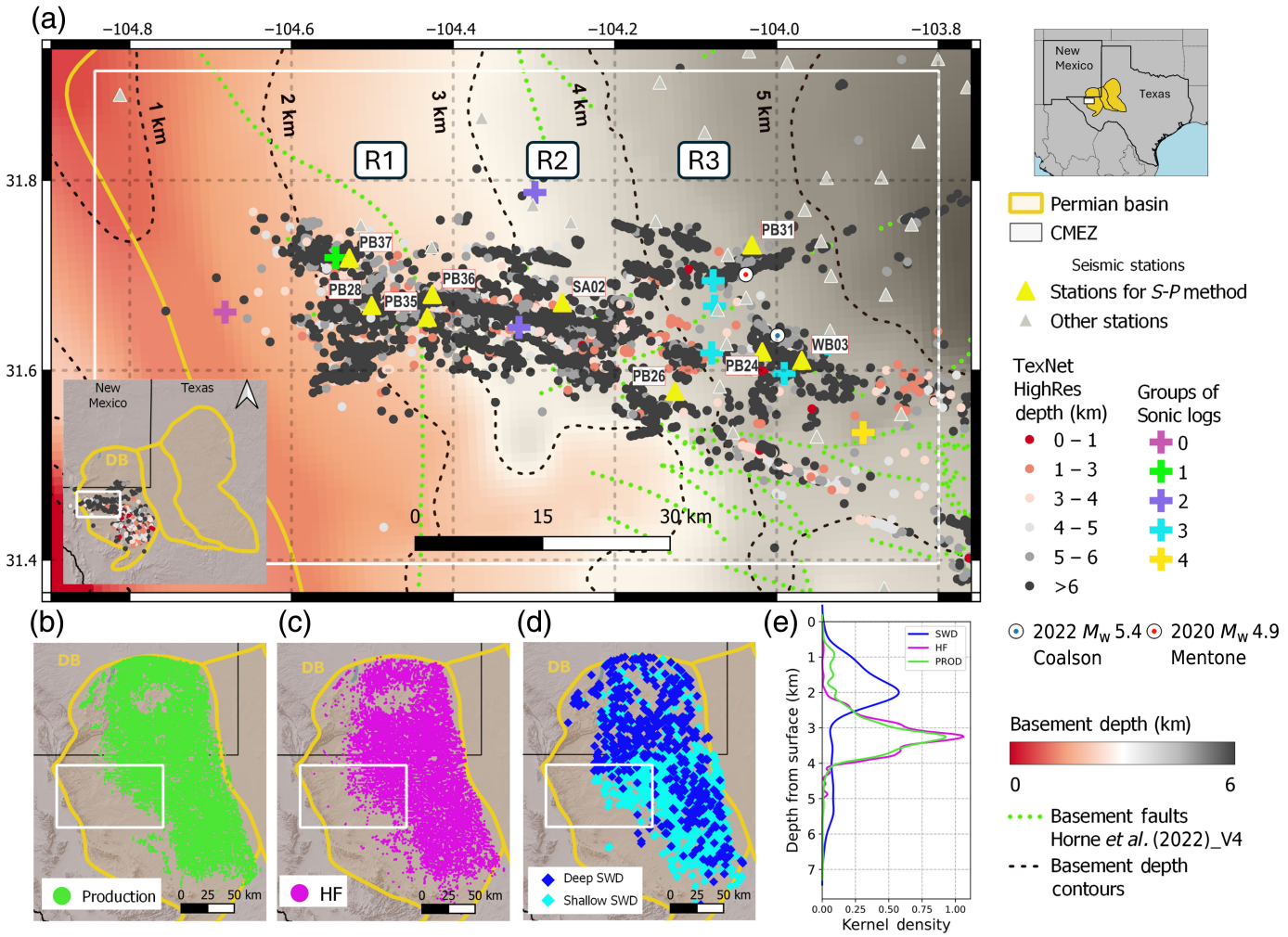

Ordovician, Silurian, and Devonian periods (Gao *et al.*, 2020), at depths between 1300 and 6000 m. These differences are based on a balance between operational efficiency and geological capacity in managing wastewater disposal.

Since 2009, reports of triggered seismicity in the DB region have highlighted the impact of injection practices on subsurface conditions (Frohlich *et al.*, 2020; Skoumal *et al.*, 2020; Skoumal and Trugman, 2021). Seismic monitoring has improved significantly since 2016 with the establishment of the TexNet seismic network in Texas (Savvaidis *et al.*, 2019), providing clearer evidence of induced seismicity. TexNet produces two earthquake catalogs in DB, both assuming a 1D velocity model (DB1D) with a fixed V_P/V_S ratio of approximately 1.75 in each layer (Huang *et al.*, 2017; Savvaidis *et al.*, 2019). The first catalog is based on NonLinLoc, a probabilistic earthquake location algorithm that determines absolute earthquake locations (Lomax *et al.*, 2000). The second, the high-resolution earthquake catalog (HighRes), is based on GrowClust, a relative relocation method that refines earthquake positions using initial reference locations and waveform cross correlation (Trugman and Shearer, 2017). TexNet HighRes offers improved resolution, particularly in the horizontal (x and y) directions, enhancing the imaging of fault-zone structures.

Figure 1. Seismicity in the Culberson–Mentone earthquake zone (CMEZ), Delaware basin (DB). (a) Map of earthquakes in the CMEZ from the TexNet high-resolution catalog, with events colored by depth with respect to sea level. Seismic stations highlighted on the map were selected for analysis due to their proximity to a sufficient number of earthquakes. The map also shows the depth of the basement relative to sea level with contour lines, defining regions R1, R2, and R3. It shows the locations of sonic logs (grouped by similarity) and highlights two significant earthquakes: 2022 M_w 5.4 Coalson and 2020 M_w 4.9 Mentone. (b–d) Spatial distribution of wells associated with (b) hydrocarbon production in the DB, (c) hydraulic fracturing (HF), and (d) shallow and deep saltwater disposal (SWD). (e) Kernel density plot showing the depth distribution of operational activities across the DB. The color version of this figure is available only in the electronic edition.

Figure 1a presents the HighRes catalog in the western DB, specifically within the Culberson–Mentone earthquake zone (CMEZ), located in the northern Delaware basin earthquake zone (NDBEZ) (Smye *et al.*, 2024). The CMEZ includes part of Culberson and Reeves Counties in Texas, where two notable earthquakes have occurred: the M_w 4.9 "Mentone" earthquake (initially reported as M_w 5.0) in 2020 and the M_w 5.4 "Coalson

Draw" earthquake in late 2022. The mechanisms and implications of these events have been the focus of several studies (Hennings *et al.*, 2021; Skoumal *et al.*, 2021; Tung *et al.*, 2021; Bolton *et al.*, 2024; Tan and Lui, 2024). The HighRes catalog reveals earthquake lineations trending northwest–southeast, roughly parallel to crystalline basement faults. Most of the events occur at depths 6 km below sea level (7.1 km below the surface) and form a diffuse seismic cluster with no clear depth trend. These events are located primarily within the crystalline basement, significantly deeper than the known fluid injection zones in the region.

Accurate estimation of hypocentral depths is essential for identifying the causal mechanisms of induced seismicity and distinguishing between different operational sources, which typically occur in distinct geological formations at different depths. However, estimating earthquake depths in the DB remains challenging due to the region's complex subsurface structure (Lomax and Savvaidis, 2019; Abubakar *et al.*, 2022; Sheng *et al.*, 2022). This challenge is particularly pronounced for CMEZ, in which both formation and basement stratigraphy vary significantly along the longitudinal axis (Fig. 1a), indicating strong lateral heterogeneity in *P*- and *S*-wave velocities. This heterogeneity introduces uncertainties in depth estimations derived from the standard DB1D velocity model. Previous work (Sheng *et al.*, 2022) has demonstrated that accurate focal depths can be obtained using *S-P* time differences and locally constrained velocity models, especially when stations are located near the epicenters. Although this single-station approach does not benefit from multiple seismic paths, it reduces the impact of complex ray paths caused by lateral velocity variations and may offer more reliable depth estimates in geologically complex regions.

This study aims to improve the accuracy of earthquake depth estimates in the CMEZ through a two-step process. The first step, referred to as the *S-P* method, focuses on events located directly beneath the seismic stations. This method uses manual observations of *S-P* time differences, the V_P/V_S ratio calculated from the observed times, and a V_P velocity model derived from local acoustic sonic logs. The second step involves relocating the remaining earthquakes using a relative relocation method, which uses the depth residuals between the HighRes and the *S-P* depths from step 1. The final product is the *S-P* high-resolution catalog for CMEZ (*S-P* HighRes), which combines the results from both steps. This catalog includes the same earthquakes as the HighRes catalog (from May 2017 to April 2024) but with more accurate depth estimates. The relocated earthquake depths are located below the basin–basement interface and show two clear trends: they gradually increase in depth from west to east, following the deepening basement structure, and tend to occur at greater depths over time. This enhanced depth resolution is expected to provide valuable insights into the mechanisms driving induced seismicity in the CMEZ.

Data Sources

Crustal structure

Figure 1 illustrates a west-to-east deepening of the basement, indicating a similar trend in the overlying formations and overall crustal structure. This gradient suggests that the DB1D model may introduce biases in this region, potentially affecting the accuracy of earthquake depth estimates. The effect is especially pronounced in regions R1, R2, and R3, which are defined by the basement depth contours. In these regions, the basement top varies rapidly from 2 to 5 km, and they also contain the majority of HighRes earthquake locations in the CMEZ.

To reduce these biases and improve depth resolution, localized 1D *P*-wave velocity models were developed for the CMEZ using sonic log data and corresponding formation information provided by Enverus (2025) (Fig. 2a–e). The logs were grouped from 0 to 4 by region based on the basement topography contours (Fig. 1a), except for the log with API 42-389-32460-00-00. Although located in region R3, this log is spatially distant from others in the same region but in the deepest part of the basin studied (Fig. 2e). Median velocities were calculated every 0.1 km to construct representative velocity models for each well. Although the acoustic logs only extend to certain depths, stratigraphic correlations and velocity contrasts suggest that most logs reach nearly to the top of the basement. Where the sonic logs end, we assume a basement velocity of 6 km/s.

The resulting velocity models and formation data confirm the west-to-east deepening trend, consistent with regional structural dip or thickening of sedimentary units. Moreover, the stratigraphy shows a high degree of lateral continuity across the groups, especially in the zones defined by velocity marked A through D in Figure 2. These zones were identified based on consistent velocity contrasts and formation boundaries. Although we do not attempt a detailed stratigraphic analysis, our focus is to examine how the average velocities from the surface to the basement affect the estimated depths of the earthquakes. The localized models highlight the need for detailed velocity structure in the CMEZ; especially in the east–west direction, to better resolve earthquake depths and account for rapid subsurface variations.

Earthquake data

TexNet provides two earthquake catalogs for the CMEZ, both using the same DB1D velocity model (Figs. S1 and S2, available in the supplemental material to this article). One catalog was generated using NonLinLoc, based on absolute earthquake locations, whereas the other was produced using GrowClust, which refines relative locations. The NonLinLoc catalog yields reliable horizontal (x–y) earthquake locations, with most events occurring at depths between 7 and 10 km below sea level (Fig. S1a,b). In contrast, the GrowClust catalog enhances the clarity of earthquake lineations, particularly those trending northwest–southeast, providing a sharper image of fault-zone structures. Earthquakes in this catalog are generally shallower,

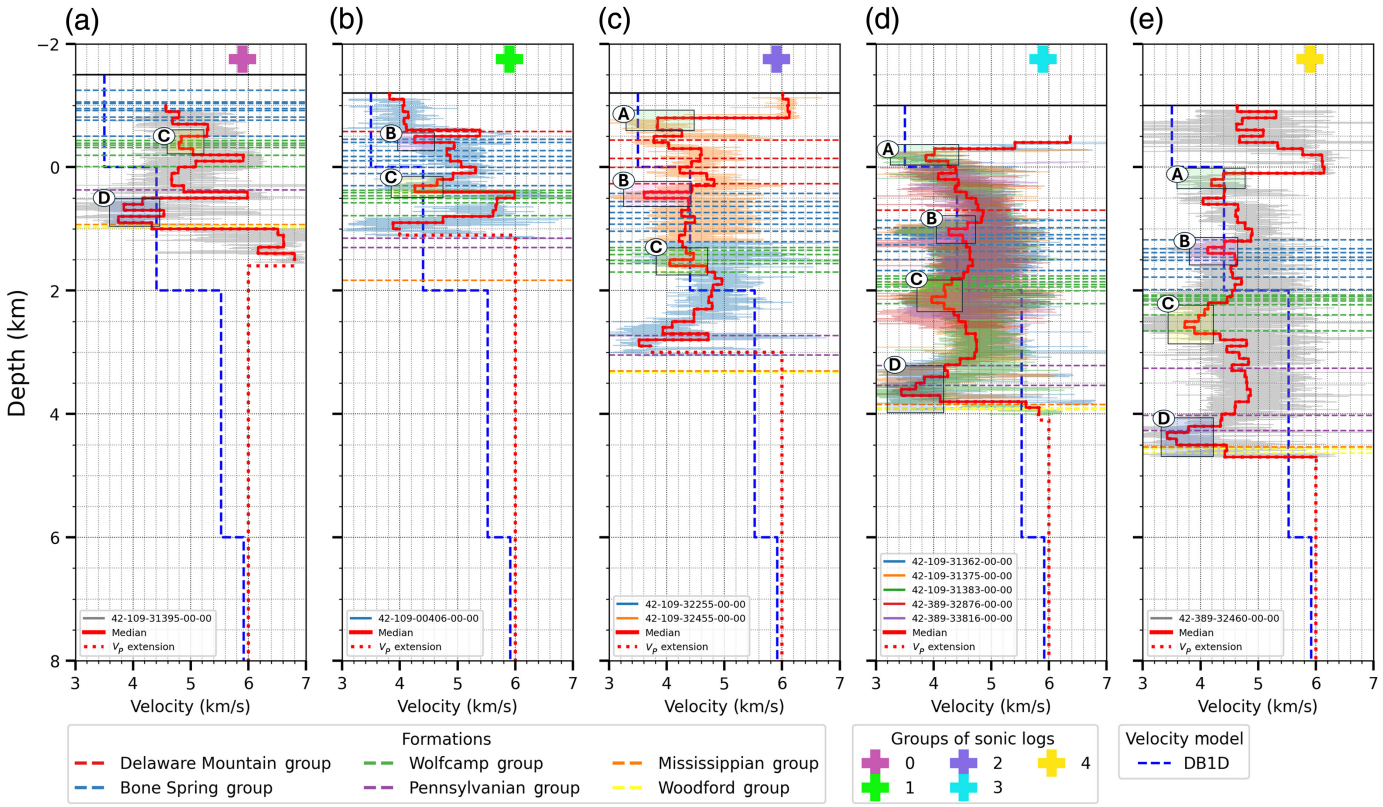

Figure 2. Sonic velocity profiles from wells in the CMEZ, showing *P*-wave velocity variations across geological formations (horizontal dashed lines at different tops) and sonic log groups (0–4), arranged from west to east. Zones A–D reflect velocity contrasts correlated on each log group. The continuous red line represents the median V_P model, calculated every 0.1 km from sonic logs (raw data in the back), whereas its extension indicates the basement velocity. The DB1D velocity model (blue-dashed line) is included for comparison. (a) Group 0, located in the western CMEZ. (b–d) Groups 1, 2, and 3, corresponding to well logs in regions R1, R2, and R3, respectively. (e) A well log in southeastern CMEZ (region 3), from the deepest part of the basin studied. The color version of this figure is available only in the electronic edition.

ranging from 5 to 8 km in depth (Fig. S2b). An exception to this pattern is the Culberson earthquake zone, in which events reach higher depths up to 11 km in the NonLinLoc catalog and 10 km in the GrowClust catalog.

We used the TexNet HighRes catalog (Texas Seismological Network and Seismology Research at University of Texas at Austin, 2025) to perform our sensitivity analysis in CMEZ. The catalog spans from May 2017 to April 2024, revealing a clear increase in the number of earthquakes with magnitudes greater than 2 over time (Fig. 3), and recording important earthquakes such as the Mentone earthquake (initially M_w 5.0, later reported as 4.9 in the HighRes catalog) in 2020 and the Coalson earthquakes (M_w 5.4 in 2022 and M_w 5.2 in 2023). Earthquakes with magnitudes below 2 are also observed in certain periods (Figs. S1c,S2c), likely due to changes in the geometry of the network (Fig. S4). In addition, some smaller events may have been detected because they occurred closer to seismic stations.

S-P Depth Relocation Method

S-P time differences ($t_S - t_P$) can be used to constrain earthquake focal depths for events occurring directly below seismic stations when the velocity structure is known. This approach has previously been applied in the southeast Delaware basin region (SEDB) to reveal shallow seismicity, particularly within the DMG formation (Sheng *et al.*, 2022) (Fig. S5). In this study, we present the *S-P* method with the goal of not only estimating the maximum possible depth but also recovering the actual focal depth of earthquakes.

The method estimates earthquake depth based on the time difference between *S*- and *P*-wave arrivals ($t_S - t_P$), the ratio of *P*- to *S*-wave velocities (V_P/V_S), and the average *P*-wave velocity V_P along the source-to-station path. The depth, z, is given by

$$z = \frac{t_S - t_P}{V_P/V_S - 1} V_P, \tag{1}$$

which is valid for earthquakes located approximately beneath the recording station, in which arrivals are manually identified and the velocity values reasonably approximate the true path-averaged structure.

Given the high horizontal (x–y) accuracy of the HighRes catalog, we rely on these coordinates and apply the *S-P* time method to estimate earthquake depths. In addition to their

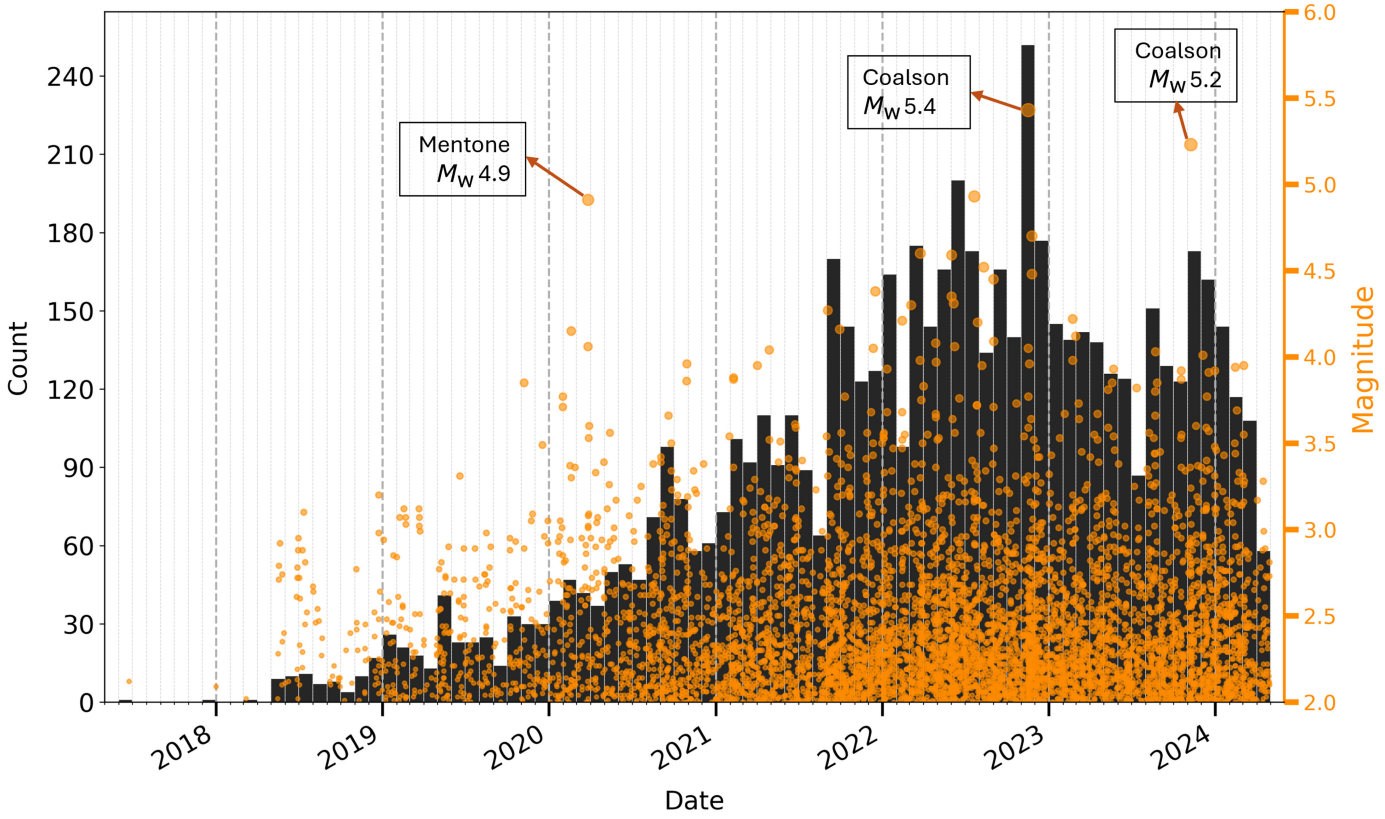

Figure 3. High-resolution earthquake distribution in the CMEZ from 2017 to 2024 for events with magnitudes greater than 2. Notable events show M_w 4.9 Mentone earthquake in 2020 and two Coalson earthquakes of M_w 5.4 and M_w 5.2 in 2022 and 2023, respectively. The color version of this figure is available only in the electronic edition.

accuracy, we note that HighRes epicentral locations typically differ by only about 1 km from those obtained with NonLinLoc (Fig. S3), providing confidence in the epicentral positions used in this study.

To ensure the robustness of our depth estimates, we restrict the analysis to earthquakes occurring within 3 km of each station and for which both *P*- and *S*-wave arrivals are available. This 3 km threshold was selected based on the distribution of *S-P* travel times, with the intent of limiting the method to events that are likely to occur nearly vertically below the station. We acknowledge that not all earthquakes are perfectly vertical relative to a station, and this assumption introduces some uncertainty in depth. However, the 3km radius reflects a practical balance between reducing horizontal offset and maintaining a sufficient number of events for analysis.

The V_P/V_S ratio was estimated from travel-time differences, and the average V_P value was obtained from velocity models derived from the sonic logs. For earthquakes in the HighRes catalog that did not meet the criteria for the *S-P* method, a relative depth relocation technique was applied to obtain their focal depths. The *S-P* HighRes Catalog combines depth estimates derived from both the *S-P* method and the relative relocation technique.

S-P time observations

We analyzed *S-P* time differences at stations whose recorded events were within 1–5 km of radius (Fig. S6). Regardless of the chosen radius, the observed trend remains consistent: *S-P* time differences are generally larger at stations in the eastern part of the CMEZ compared with those in the west. Although some stations recorded some events within the first 2 km, we found that 3 km offered the best trade-off between capturing a sufficient number of events and ensuring that earthquakes were approximately located beneath the stations.

Figure 4a shows the statistical distribution of *S-P* time differences for earthquakes occurring within 3 km of seismic stations that recorded a sufficient number of events under this condition. The results consistently show larger *S-P* time differences in the eastern CMEZ, with values of approximately 1 s at the western station in region R1 and 1.3 s at the eastern station in region R3. The *S-P* differences in the CMEZ are significantly higher compared with those in the SEDB, which are around 0.6 s (Fig. S6), suggesting deeper seismicity beneath the CMEZ.

In addition, the west-to-east seismicity depth trend in CMEZ, combined with the assumption of constant average *P*- and *S*-wave velocities (V_P and V_S) throughout the region, could indicate a deepening of seismicity from west to east (equation 1). However, given the complex geology of the CMEZ basin,

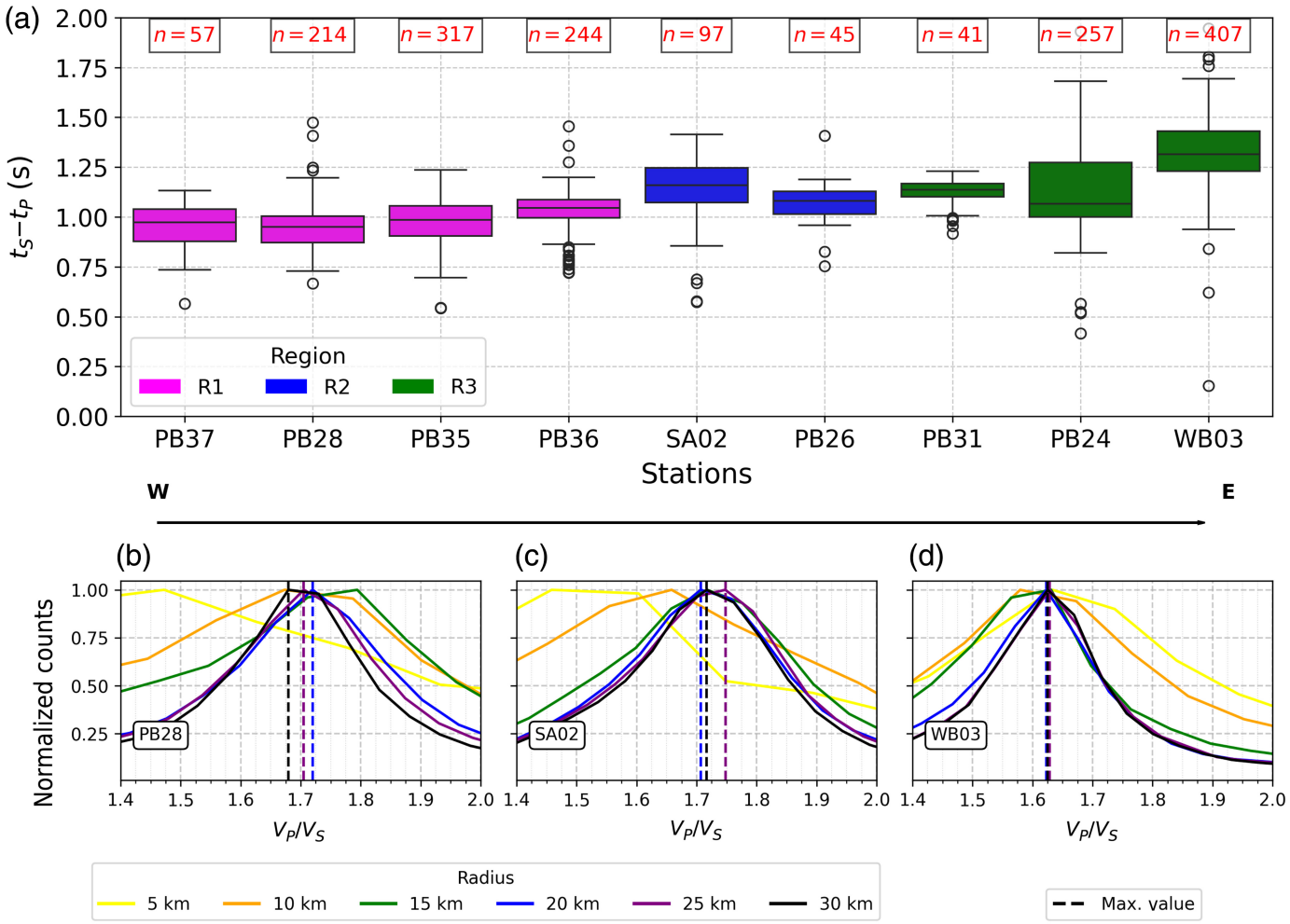

Figure 4. (a) Box plots of travel-time differences ($t_S - t_P$) for earthquakes within 3 km epicentral distance of stations in the CMEZ, ordered west to east (W to E). The station colors indicate their corresponding regions (R1–R3). Event counts are shown above each station. (b–d) Normalized frequency distributions of V_P/V_S ratios at stations PB28, SA02, and WB03, respectively, for radii ranging from 5 to 30 km. The dashed lines indicate the maximum V_P/V_S values for the 20, 25, and 30 km radii. The color version of this figure is available only in the electronic edition.

variations in V_P and V_S across the region are also likely and must be considered when interpreting these results.

V_P/V_S ratio

Dipole sonic logs were not available for the study area, limiting the resolution of V_S compared with V_P. However, the *S-P* location method allows us to estimate the depths assuming that the V_P/V_S ratio is known (equation 1). Therefore, we calculated this ratio taking advantage of *P* and *S* observations again, but this time using pairs of *P* and *S* arrival times (Lin and Shearer, 2007; Palo *et al.*, 2016; Sheng *et al.*, 2022).

To estimate the V_P/V_S ratio in CMEZ, we use wave travel-time differences from two configurations (Fig. S7): (1) earthquake pairs recorded at the same station, and (2) a single earthquake recorded at two different stations. Both approaches rely on the assumption that seismic waves travel along paths with similar average velocities.

Figure 4b–d shows the V_P/V_S analysis for three stations located in regions R1, R2, and R3, obtained using method 1. The analysis was performed by varying the radius of the station–event in 5 km increments from 5 to 30 km, considering all earthquake pairs within each distance threshold. We adopted a 30 km station–event radius and a 30 km interevent distance limit because these values provide an effective balance between statistical robustness and local spatial resolution. Analyses for the remaining stations are presented in Figure S8. This method was also applied to the SEDB (Fig. S9), producing V_P/V_S ratios similar to those reported by Sheng *et al.* (2022), who used method 2 in their analysis.

Method 2 consists of obtaining arrival times from a single earthquake recorded at two different stations. We performed this analysis for earthquakes and stations in each of the three regions. Overall, both methods produced V_P/V_S ratios in regions R1 and R2 of approximately 1.70–1.73 (Fig. S10), close to the 1.75 value reported in DB1D. However, in region R3, method 1 produced a noticeably lower V_P/V_S ratio, ranging

from approximately 1.62 to 1.65. This discrepancy likely arises because both DB1D and method 2 consider broader regional data, which can average out localized variations. In contrast, method 1 focuses on individual stations, such as WB03 and PB24, which are located in areas of high seismicity like the Culberson and Mentone zones. The large number of earthquake pairs in these areas allows method 1 to converge quickly on the V_P/V_S ratio, even at a station–event radius of just 5 km, providing a more localized and accurate estimate. Consequently, all subsequent analyses are based exclusively on results from method 1.

Because the *S-P* time differences and the average velocity model were obtained from observed data, the V_P/V_S ratio is the parameter with the largest uncertainty in the *S-P* method for the CMEZ. To quantify this uncertainty, we performed a bootstrap analysis for each earthquake.

For each earthquake, we computed 1000 bootstrap V_P/V_S medians, which were then used to generate 1000 corresponding bootstrap depths, providing an estimate of the depth uncertainty for the event. An example of the bootstrapping procedure is shown in Figure S11. The analysis consists of two main steps. 1. Cleaning V_P/V_S values (Fig. S11a–c): for each station, raw V_P/V_S values were cleaned by removing outliers and then windowed around the mode within one standard deviation. 2. Bootstrapping (Fig. S11d–f): we performed 1000 bootstrap iterations of V_P/V_S values and the corresponding earthquake depths, drawing 1000 samples in each iteration. The median of the bootstrap depths was taken as the final depth estimate, and the range of the bootstrap results was used to quantify the associated uncertainty.

Depth of Seismicity

S-P depth location

In the CMEZ region, *S-P* time observations increase from west to east, suggesting a corresponding increase in earthquake depth in that direction. The V_P/V_S ratio also exhibits a spatial trend, decreasing from approximately 1.7 in the west to about 1.65 in the east. This pattern is supported by sonic log data and formation information, which confirm a west-to-east deepening trend.

The average *P*-wave velocity (V_P) represents the final input required to estimate earthquake depths using equation (1). Figure 5 illustrates how the average V_P varies with depth, calculated as $V_P = \sum_{i=1}^{N} z_i V_{P_i}$, in which V_{P_i} is the *P*-wave velocity from sonic log data for layer *i*, and z_i is the corresponding thickness.

Using the interquartile range of the *S-P* times and the corresponding V_P/V_S ratios, we delineated a shaded polygon in Figure 5 that intersects the average V_P curve, representing the depth range corresponding to the central 50% of the calculated earthquake depths. This visualization confirms the east-to-west deepening trend and also enables comparison of earthquake depths under different velocity models.

In region R1, differences between the average V_P from the DB1D model and our derived velocity model result in depth estimates that differ by approximately 1 km when applying the *S-P* method. Specifically, our model places the central 50% of the earthquake depths between 6 and 7 km below sea level, whereas the DB1D model suggests shallower depths between 5 and 6 km. In contrast, for regions R2 and R3, where earthquakes are generally deeper, both models produce similar average velocities after 3 km below sea level, resulting in comparable depth estimates. For region R2, central depths range from 6.5 to 8 km below sea level, whereas in region R3 they range from 7 to 11 km. This consistency implies that, in these deeper regions, earthquake depths are primarily controlled by the *S-P* time and the V_P/V_S ratio, rather than by variations in the velocity model. We further explore the implications of these findings in the uncertainties and limitations part of the discussion.

Relative depth relocation

Earthquake depths directly beneath stations were estimated using the *S-P* method. For the remaining events, a relative relocation approach based on weighted depth residuals from spatial neighbors was applied (see Algorithm 1 in the supplemental material). This method leverages nearby events with known depths; derived from both the *S-P* method and the HighRes catalog, to estimate missing values. For each event that lacks the depth of the *S-P* method, the algorithm identifies neighboring reference events that have both original and updated depths, computes the residual corrections, and applies a weighted average of these corrections using inverse distance weighting. The final depth is obtained by adding this correction to the original catalog depth. This spatially guided strategy enables consistent reasonable relocation of event depths in which direct *S-P*-based estimates are unavailable.

The *S-P* HighRes catalog integrates data from both the *S-P* method and the relative depth relocation approach. Figure 6 illustrates a cross plot of seismicity in the CMEZ, comparing the *S-P* HighRes catalog with the TexNet HighRes catalog. Unlike the HighRes catalog, the *S-P* HighRes Catalog reveals that seismicity deepens from west to east, aligning with the basement trend, with depths ranging from 4 to 9 km below sea level in region R1, 5–10 km in region R2, and 6–12 km in region R3. Despite these differences in depth gradients, both catalogs consistently indicate that the CMEZ hosts relatively deep seismicity.

Across the entire CMEZ, both catalogs indicate a primary seismicity concentration between 6 and 7 km from sea level. However, the *S-P* HighRes catalog shows a slightly lower peak due to the influence of deeper events; particularly in R3, in which the largest magnitude earthquakes associated with the Mentone sequence are concentrated.

Discussion

Spatial analysis of earthquake depths

Seismicity in the CMEZ of the NDBEZ is notably complex, characterized by deep events that do not show a direct correlation between depth and oil and gas activity. Although SWD is

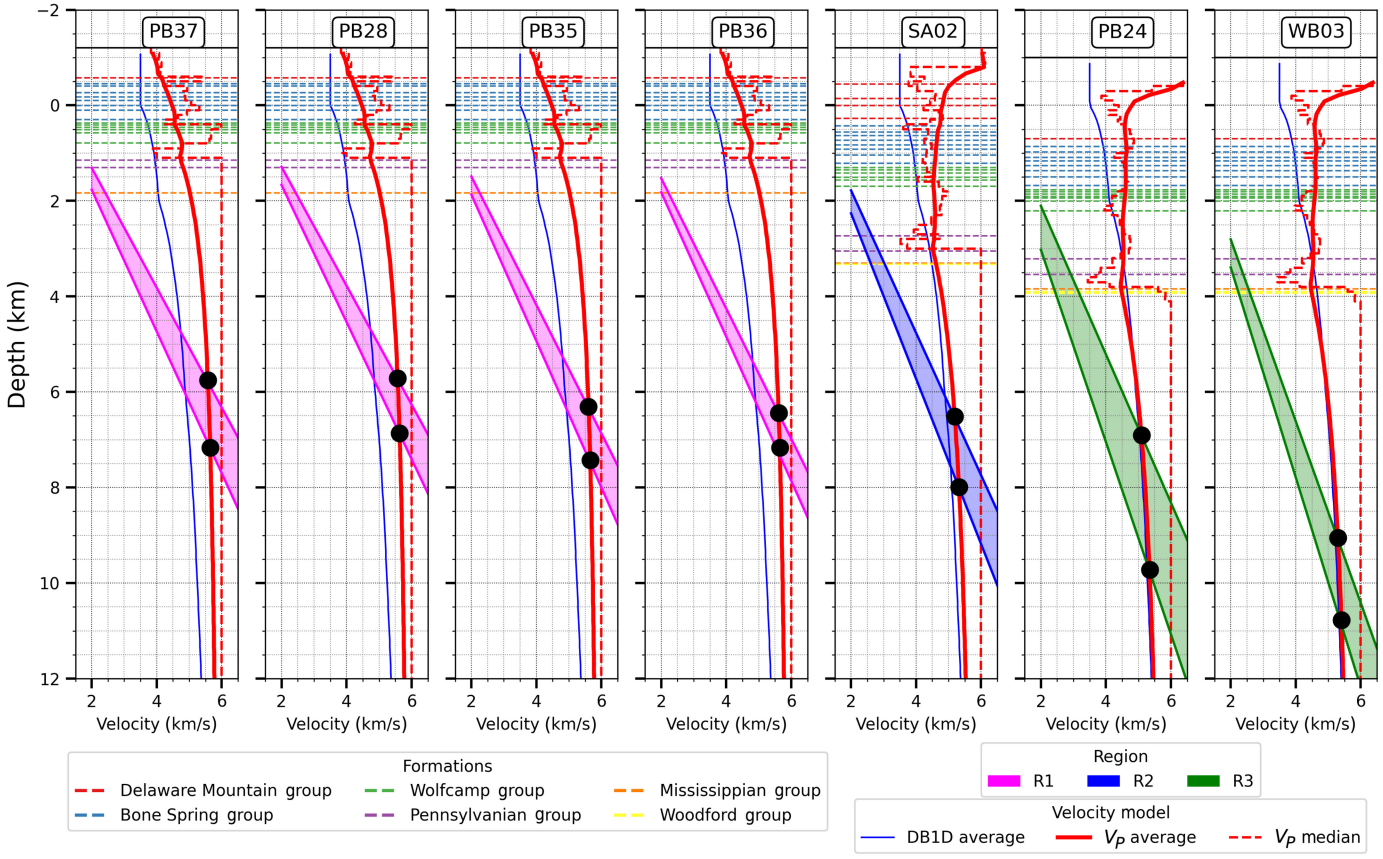

Figure 5. Estimated seismicity depth ranges at stations in the CMEZ. The vertical solid lines show average *P*-wave velocity (V_P) as a function of depth for two models: DB1D (blue) and the station-specific derived model (red). The shaded polygons, colored according to each station's region, show the depth ranges computed using equation (1), based on the interquartile range of *S-P* times and the corresponding V_P/V_S ratios. The intersection of each polygon with the average V_P curve indicates the approximate depth range encompassing the central 50% of the calculated earthquake depths. The color version of this figure is available only in the electronic edition.

widely recognized as a key driver of induced seismicity in the DB (Lomax and Savvaidis, 2019; Savvaidis *et al.*, 2020; Dvory and Zoback, 2021; Skoumal and Trugman, 2021; Zhai *et al.*, 2021; Smye *et al.*, 2024); primarily through increased pore pressure in subsurface formations, the relative contributions of shallow versus deep injection remain under debate, emphasizing the need to clarify the underlying physical mechanisms. Although the SEDB is typically associated with shallow injection-related seismicity (Savvaidis *et al.*, 2020; Hennings *et al.*, 2021; Abubakar *et al.*, 2022; Sheng *et al.*, 2022), seismicity in the CMEZ is thought to be driven mainly by deep injection (Dvory and Zoback, 2021; Hennings *et al.*, 2021; Grigoratos *et al.*, 2022; Smye *et al.*, 2024), due to the close vertical proximity of injection zones to the top of the crystalline basement.

The *S-P* HighRes catalog confirms that seismicity occurs beneath the basement and reveals a previously unrecognized deepening trend parallel to the basement surface. Because of the lack of a dense seismic network and an accurate 3D velocity model, this trend was not captured fully by earlier TexNet catalogs, including NonLinLoc and HighRes. The *S-P* HighRes catalog was constructed using two complementary methods: one based on *S-P* time observations combined with local velocity models derived from acoustic logs, and the other employing a relative relocation method. By incorporating the longitudinal heterogeneity in the basement topography and overlying stratigraphy, the catalog offers enhanced resolution and highlights the influence of structural variability on the velocity model.

The seismicity observed beneath and parallel to the top of the basement suggests a significant mechanical contrast between the overlying sedimentary cover and the crystalline basement. This contrast favors the reactivation of pre-existing, optimally oriented basement-rooted faults under elevated pore pressure conditions (Huang *et al.*, 2022). These faults may propagate upward and terminate near the base of the sedimentary section, serving as vertical pathways for pore pressure migration and, in some cases, hydraulic communication (Walsh and Zoback, 2015). However, such fluid connectivity is not strictly necessary; diffusion alone may be sufficient to perturb fault stability. These basement-rooted faults are particularly sensitive to pore pressure changes, largely due to their close proximity to deep SWD zones. Consequently, deep injections occurring even up to 30 km away can significantly alter

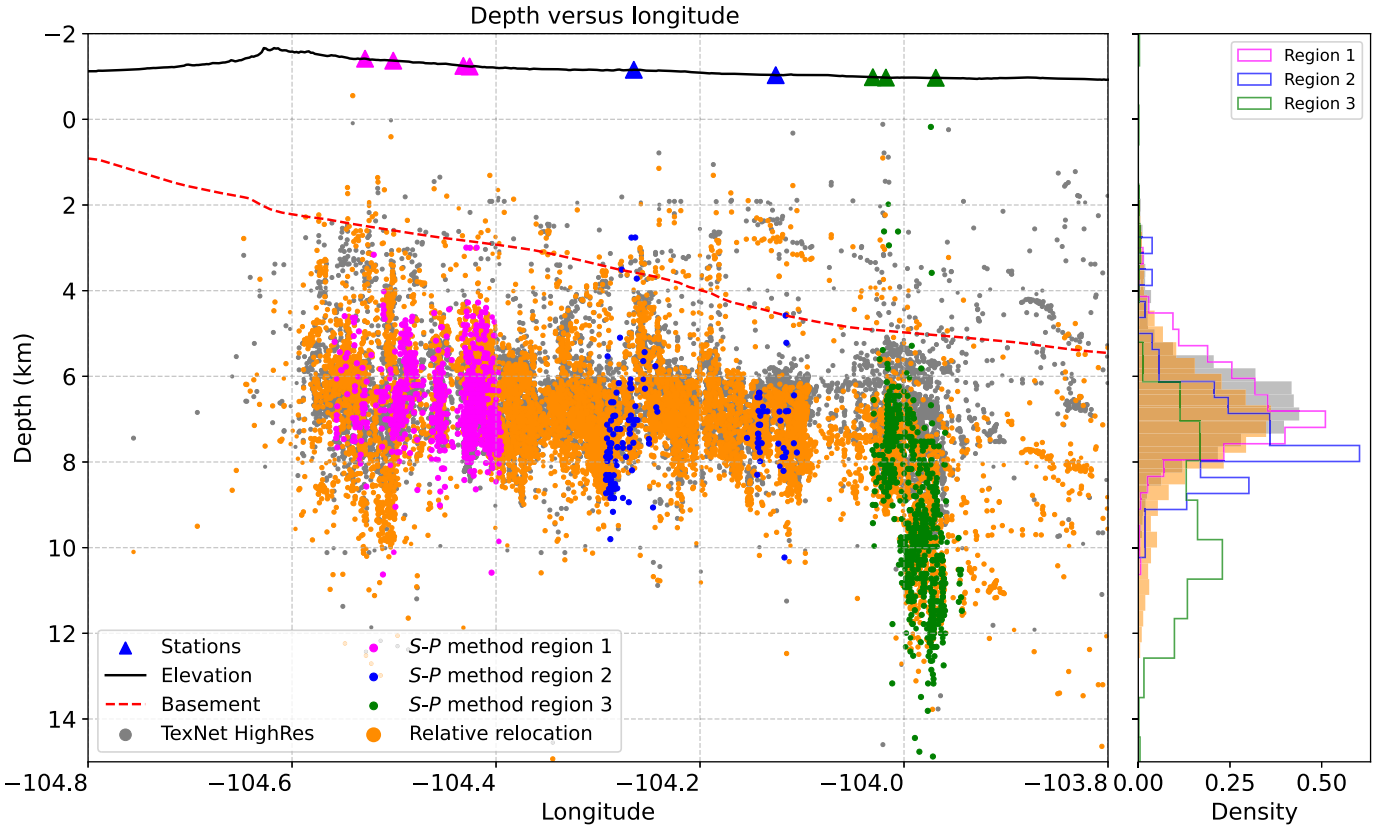

Figure 6. Cross plot of seismicity in the CMEZ. The gray points show events from the TexNet high-resolution catalog. The colored points represent the *S-P* high-resolution catalog, including earthquakes with depths estimated using the *S-P* method beneath stations in regions R1 (pink), R2 (blue), and R3 (green), and events relocated with the relative depth-correction method elsewhere (orange). The elevation profile is shown in black, and the basement depth is indicated by the red-dashed line. Depth-density distributions are plotted along the right-hand axis. The color version of this figure is available only in the electronic edition.

the effective stress regime (Smye *et al.*, 2024), triggering seismicity in the CMEZ.

Temporal analysis of earthquake depths

Temporal analysis offers important insights into the characteristics of induced seismicity (Watkins *et al.*, 2023). Accordingly, we conducted a temporal analysis to investigate the evolution of earthquake depths in the CMEZ. Figure 7 shows the depth evolution over time for each region, using the HighRes and *S-P* HighRes catalogs. In both catalogs, depth estimates show instability during the early period, up to early 2020. This is likely due to limitations of the geometry of the seismic network. The HighRes catalog is particularly affected due to its reliance on double-difference relocation methods, whereas the *S-P* HighRes catalog inherits similar limitations because it uses the epicentral locations from HighRes as a base.

From 2020 onward, both catalogs exhibit more stable and reliable trends in CMEZ, likely resulting from improved detectability with the addition of stations PB28, PB29, and PB33 (Fig. S4). Notably, there is a progressive deepening of earthquake hypocenters over time (Video S12), especially in regions R1 and R3, whereas region R2 remains comparatively stable (Fig. 7). The deepening observed in R1 and R3 suggests downward migration of pore pressure fronts, consistent with ongoing propagation into deeper fault segments (Shapiro *et al.*, 1997; Layland-Bachmann *et al.*, 2012; Goebel *et al.*, 2017; Savvaidis *et al.*, 2020; Smye *et al.*, 2024). This may help explain the increased susceptibility of these regions to moderate-to-large magnitude earthquakes. These patterns are more clearly visible in the *S-P* HighRes catalog, which offers improved depth resolution and captures distinct depth distributions across the regions.

Another notable feature captured by the *S-P* HighRes catalog is the greater dispersion in earthquake depths compared with the TexNet HighRes catalog. This increased variability reflects differences in *S-P* arrival-time observations, which may be affected by event–station geometry—particularly when events are not directly beneath seismic stations—or by natural variability, such as the aftershock sequences following the Coalson events in region R3 during late 2023 (Fig. S13).

Beyond pore pressure migration, other factors such as distance from deep injection zones and earthquake-to-earthquake interactions may also influence seismic behavior in the CMEZ (Chen *et al.*, 2013; Shapiro *et al.*, 2013; Catalli *et al.*, 2016; Kettlety *et al.*, 2019; Verdecchia *et al.*, 2021). Figure 7

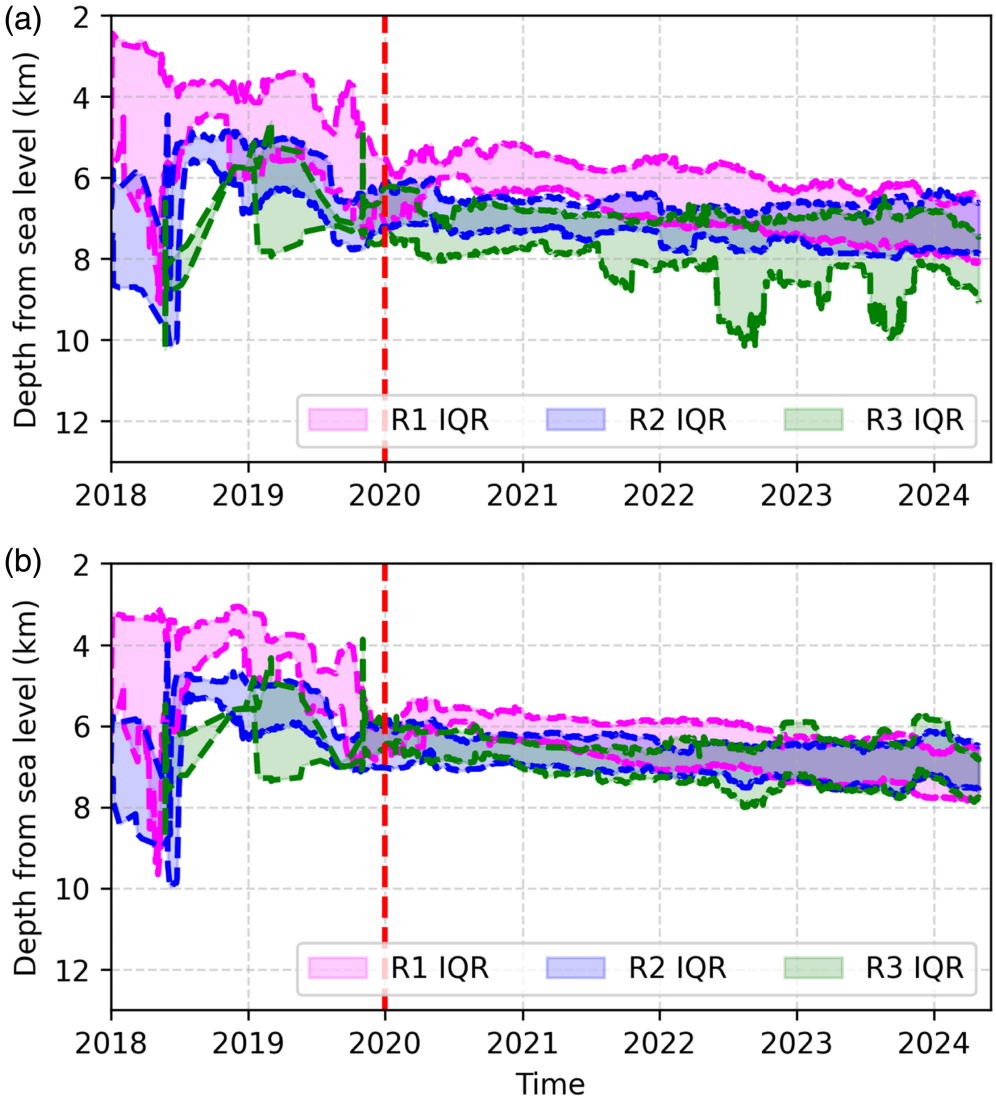

Figure 7. Earthquake depths over time by region in the CMEZ. (a) *S-P* high-resolution catalog. (b) TexNet high-resolution catalog. The shaded bands represent the interquartile range (IQR) of earthquake depths calculated using a 90-day moving window. The red vertical dashed line marks the approximate time when earthquake depths begin to stabilize. The color version of this figure is available only in the electronic edition.

highlights that region R3 exhibits the most rapidly deepening trend. This region also experienced several high-magnitude events and their associated aftershock sequences, suggesting the possibility of dynamic stress transfer. Such interactions could facilitate rupture propagation to greater depths, particularly in well-connected fault systems capable of transmitting stress efficiently.

Achieving high-resolution earthquake locations in both the epicentral and depth dimensions is essential for understanding the physical mechanisms driving induced seismicity and for improving interpretations of stress accumulation and release. This requires the use of velocity models that accurately represent the geological and physical properties of the study area. In addition, expanding the seismic network within the CMEZ—particularly by deploying stations above known seismic clusters—will improve catalog quality. Finally, continuous monitoring of earthquake depth over time provides critical insight into the evolving physical processes behind induced seismicity.

Uncertainties and limitations

The *S-P* high-resolution catalog for the CMEZ improves earthquake depth estimates, but both the *S-P* and relative relocation methods involve uncertainties and limitations. In the *S-P* method, the 3 km radius assumption is meant to ensure near-vertical ray paths for events located close to seismic stations. However, this assumption can be affected by horizontal location errors in the HighRes catalog or by the inclusion of distant events, potentially biasing depth estimates by some hundred meters. Despite this, the impact is expected to be minor because the relative differences in epicentral locations between the TexNet catalogs are typically less than 1 km (Fig. S3).

Additional uncertainty arises from manual picking of *P*- and *S*-wave arrivals. Low signal-to-noise ratios, complex waveforms or analyst subjectivity can introduce *S-P* time errors that significantly impact depth accuracy. This effect is partially mitigated by analyzing multiple events at the same station. Furthermore, the *P*-wave velocity model V_P significantly influences depth estimates in region R1 (Fig. 5). In contrast, regions R2 and R3 are primarily controlled by the *S-P* time and the V_P/V_S ratio. This is because the average *P*-wave velocity is strongly governed by the basement structure in these regions, which is consistently around 6 km/s in both the DB1D and local velocity models.

The V_P/V_S ratio represents the largest source of uncertainty in the *S-P* method for the CMEZ because it is derived from travel-time differences of earthquake pairs located within 30 km of a station and up to 30 km apart from each other.

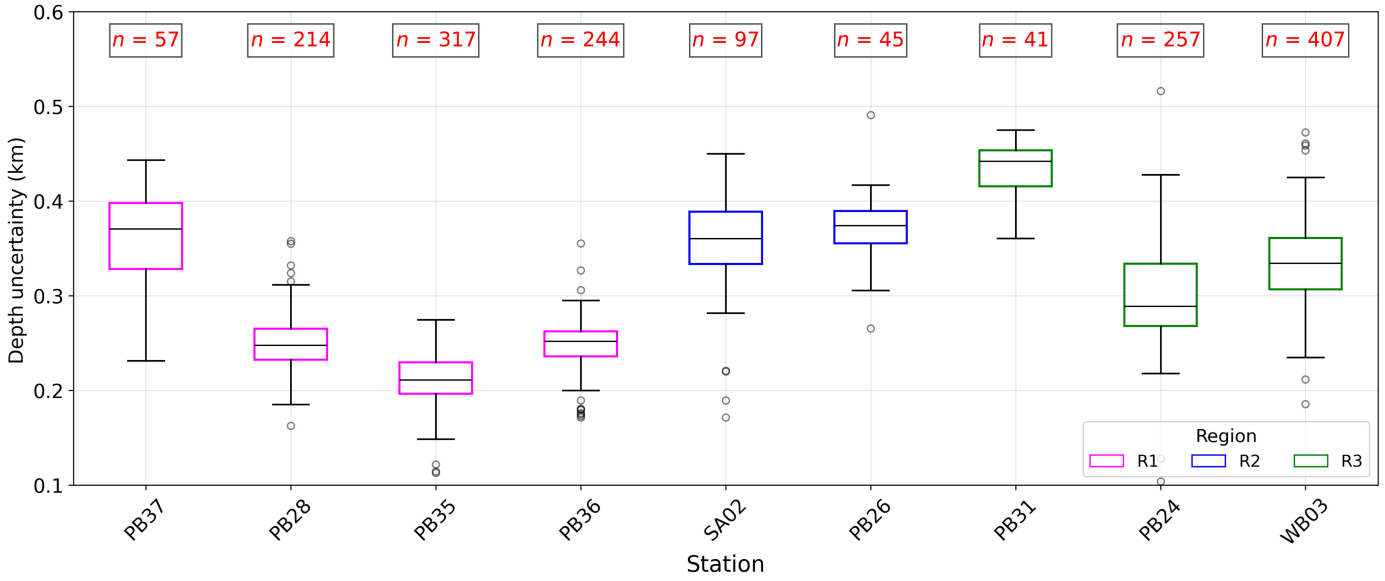

Although a 3 km radius was used for the *S-P* estimates, the V_P/V_S calculation is not limited to earthquakes directly beneath each station. Although a smaller radius would provide better local resolution, the limited number of event pairs requires a larger radius. We found that a 30 km radius provides the best balance between statistical robustness and local spatial resolution.

To further quantify this uncertainty, we performed bootstrapping of the V_P/V_S ratio to assess depth variability for each earthquake. Our results indicate that most events exhibit uncertainties less than 0.5 km (Fig. 8), reflecting the robustness of local V_P/V_S estimates derived from densely recorded earthquake pairs. As expected, events in regions with sparser station coverage or fewer nearby earthquakes, such as PB37, SA02, PB26, and PB31, show larger uncertainties, although they generally remain under 0.5 km. These findings demonstrate that the *S-P* method, when combined with bootstrapped V_P/V_S ratios, can provide reliable depth estimates across the CMEZ.

For the relative relocation method, the dependence on the reference depths is a key limitation because errors in the HighRes or the *S-P*-derived depths propagate throughout the relocation process. However, the HighRes catalog is known for its high resolution based on double-difference techniques, and the *S-P* method incorporates locally detailed information. By combining the HighRes catalog and *S-P* information, the resulting *S-P* HighRes catalog effectively captures fine-scale depth variations.

The largest source of uncertainty in the relocation method comes from the use of inverse distance weighting. This approach prioritizes nearby events, which can be effective in dense clusters but may produce inconsistent results in areas of diffuse seismicity in which neighboring events are sparse or poorly constrained. Despite these limitations, the *S-P* depth relocation method remains a robust and recommended tool for regions where epicentral locations are reliable and accurate depth estimates are needed.

Figure 8. Depth uncertainty in kilometers for events at stations in regions R1, R2, and R3 of the CMEZ. The number of earthquakes used for each station is indicated above the boxes. The color version of this figure is available only in the electronic edition.

Conclusions

We introduced the *S-P* high resolution catalog (*S-P* HighRes) for the Culberson–Mentone earthquake zone, developed to improve earthquake depth estimates with high resolution. This catalog retains the epicentral locations from the TexNet high-resolution catalog but recalculates depths using two complementary approaches: (1) the *S-P* method, applied to earthquakes located beneath seismic stations using local *S-P* arrival times, a derived V_P/V_S ratio, and an average V_P from sonic logs; and (2) a relative relocation method that estimates missing depths using weighted depth residuals from nearby events with known depths.

The *S-P* HighRes catalog reveals new spatial and temporal features not evident in previous catalogs. In particular, it captures a west-to-east deepening trend in seismicity that follows the basement topography, and it captures signs of downward migration of seismicity over time. These observations support the role of pore pressure diffusion as a key mechanism driving deep seismicity in the CMEZ, while also pointing to the influence of earthquake-to-earthquake triggering, especially along well-connected fault systems.

Overall, this study highlights the value of integrating local velocity models and *S-P* time differences to enhance depth resolution in a complex basin. Continuous earthquake depth monitoring in areas with active fluid injection is critical for understanding the evolution of induced seismicity and for improving seismic hazard assessments in the DB and similar regions.

Data and Resources

The *S-P* earthquake catalog, shapefiles, formation information, sonic log data, and Python scripts for the Culberson Mentone earthquake zone

(CMEZ) used in this study are publicly available on GitHub at https://github.com/ecastillot/CMEZ-SPHighResCatalog. Sonic logs, well-location data, formation information, and injection data were obtained from Enverus (https://www.enverus.com). The High-Resolution TexNet earthquake catalog is available at doi: 10.15781/76hj-ed46. All websites were last accessed in April 2025. Additional figures and supporting information are provided in the supplemental material.

Declaration of Competing Interests

The authors acknowledge that there are no conflicts of interest recorded.

Acknowledgments

Special thanks to Enverus for their assistance and for providing access to sonic logs, well location data, formation information, and injection data for the Delaware basin, Texas. The authors would like to thank the Texas Seismological Network and Seismology Research (TexNet) and the State of Texas that provided financial support for this publication under the University of Texas at Austin Award Number 201503664. The authors also thank TexNet for making the Texas earthquake high-resolution catalog publicly available. Thanks to Katie Smye and Peter Hennings from The Center for Injection and Seismicity Research (CISR) for providing the basement elevation data.

References

Abubakar, A., A. Hakami, A. Savvaidis, A. Lomax, R. Dommisse, C. Breton, M. Shirley, and V. O'Sullivan (2022). Induced seismicity hypocentral depth stability and sensitivity to V_P/V_S in the South Delaware basin, West Texas, *Proc. of the Second International Meeting for Applied Geoscience & Energy*, ASME, 1566–1570, doi: 10.1190/image2022-3751081.1.

Bolton, D. C., N. Igonin, Y. Chen, D. T. Trugman, A. Savvaidis, and P. Hennings (2024). Foreshocks, aftershocks, and static stress triggering of the 2020 M_w 4.8 Mentone earthquake in west Texas, *Seismica* **3,** no. 2, doi: 10.26443/seismica.v3i2.1420.

Catalli, F., A. P. Rinaldi, V. Gischig, M. Nespoli, and S. Wiemer (2016). The importance of earthquake interactions for injection-induced seismicity: Retrospective modeling of the Basel enhanced geothermal system, *Geophys. Res. Lett.* **43,** no. 10, 4992–4999.

Chen, K. H., R. Bürgmann, and R. M. Nadeau (2013). Do earthquakes talk to each other? triggering and interaction of repeating sequences at Parkfield, *J. Geophys. Res.: Solid Earth* **118,** no. 1, 165–182.

Dvory, N. Z., and M. D. Zoback (2021). Prior oil and gas production can limit the occurrence of injection-induced seismicity: A case study in the Delaware basin of western Texas and southeastern New Mexico, USA, *Geology* **49,** no. 10, 1198–1203.

Enverus (2025). Enverus, available at https://www.enverus.com/ (last accessed April 2025).

Frohlich, C., C. Hayward, J. Rosenblit, C. Aiken, P. Hennings, A. Savvaidis, C. Lemons, E. Horne, J. I. Walter, and H. R. DeShon (2020). Onset and cause of increased seismic activity near Pecos, west Texas, United States, from observations at the LAJITAS TXAR seismic array. *J. Geophys. Res.: Solid Earth* **125,** no. 1, doi: 10.1029/2019JB017737.

Gao, R., J. P. Nicot, P. Hennings, K. M. Smye, I. Pelletier, and E. Horne (2020). Preliminary hydrogeological modeling of deep injection in the Delaware basin for pore pressure characterization with application to induced seismicity, *AGU Fall Meeting Abstracts*, 2020, MR019–0008.

Ge, J., J.-P. Nicot, P. Hennings, K. Smye, S. Hosseini, R. Gao, and C. Breton (2022). Recent water disposal and pore pressure evolution in the Delaware mountain group, Delaware basin, southeast New Mexico and west Texas, USA, *J. Hydrol.: Regional Studies* **40,** 101041, doi: 10.1016/j.ejrh.2022.101041.

Goebel, T., M. Weingarten, X. Chen, J. Haffener, and E. Brodsky (2017). The 2016 M_w 5.1 Fairview, Oklahoma earthquakes: Evidence for long-range poroelastic triggering at > 40 km from fluid disposal wells, *Earth Planet. Sci. Lett.* **472,** 50–61.

Grigoratos, I., A. Savvaidis, and E. Rathje (2022). Distinguishing the causal factors of induced seismicity in the Delaware basin: Hydraulic fracturing or wastewater disposal? *Seismol. Res. Lett.* **93,** 2640–2658.

Hennings, P., N. Dvory, E. Horne, P. Li, A. Savvaidis, and M. Zoback (2021). Stability of the fault systems that host-induced earthquakes in the Delaware basin of west Texas and southeast New Mexico, *Seism. Rec.* **1,** no. 2, 96–106.

Huang, D., C. Aiken, A. Savvaidis, B. Young, and J. I. Walter (2017). Improving the velocity structure in the Delaware basin of West Texas for seismicity monitoring, *AGU Fall Meeting Abstracts*, 2017, S23C–0836.

Huang, G. D., E. Horne, F. Kavoura, and A. Savvaidis (2022). Characteristics of seismogenic structures and 3D stress state of the Delaware basin of west Texas as constrained by earthquake source mechanisms, *Seismol. Res. Lett.* **93,** no. 6, 3363–3372.

Kettlety, T., J. P. Verdon, M. J. Werner, J. M. Kendall, and J. Budge (2019). Investigating the role of elastostatic stress transfer during hydraulic fracturing-induced fault activation, *Geophys. J. Int.* **217,** no. 2, 1200–1216.

Layland-Bachmann, C., S. Wiemer, B. Goertz-Allmann, and J. Woessner (2012). Influence of pore-pressure on the event-size distribution of induced earthquakes, *Geophys. Res. Lett.* **39,** 9302.

Lemons, C. R., G. McDaid, K. M. Smye, J. P. Acevedo, P. H. Hennings, D. A. Banerji, and B. R. Scanlon (2019). Spatiotemporal and stratigraphic trends in salt-water disposal practices of the Permian basin, Texas and New Mexico, United States, *Environ. Geosci.* **26,** no. 4, 107–124.

Lin, G., and P. Shearer (2007). Estimating local V_P/V_S ratios within similar earthquake clusters, *Bull. Seismol. Soc. Am.* **97,** no. 2, 379–388.

Lomax, A., and A. Savvaidis (2019). Improving absolute earthquake location in west Texas using probabilistic, proxy ground-truth station corrections, *J. Geophys. Res.: Solid Earth* **124,** no. 11, 11,447–11,465.

Lomax, A., J. Virieux, P. Volant, and C. Berge-Thierry (2000). Probabilistic earthquake location in 3D and layered models, in *Advances in Seismic Event Location. Modern Approaches in Geophysics*, C. H. Thurber and N. Rabinowitz (Editors), Vol. 18, Springer, Dordrecht, The Netherlands, doi: 10.1007/978-94-015-9536-0_5.

Palo, M., F. Tilmann, and B. Schurr (2016). Applicability and bias of V_P/V_S estimates by P and S differential arrival times of spatially clustered earthquakes, *Bull. Seismol. Soc. Am.* **106,** no. 3, 1055–1063.

Savvaidis, A., A. Lomax, and C. Breton (2020). Induced seismicity in the Delaware basin, West Texas, is caused by hydraulic fracturing and wastewater disposal, *Bull. Seismol. Soc. Am.* **110,** no. 5, 2225–2241.

Savvaidis, A., B. Young, G. D. Huang, and A. Lomax (2019). Texnet: A statewide seismological network in Texas, *Seismol. Res. Lett.* **90,** no. 4, 1702–1715.

Shapiro, S. A., E. Huenges, and G. Borm (1997). Estimating the crust permeability from fluid-injection-induced seismic emission at the KTB site, *Geophys. J. Int.* **131,** no. 2, F15–F18.

Shapiro, S. A., O. S. Krüger, and C. Dinske (2013). Probability of inducing given-magnitude earthquakes by perturbing finite volumes of rocks, *J. Geophys. Res.: Solid Earth* **118,** no. 7, 3557–3575.

Sheng, Y., K. S. Pepin, and W. L. Ellsworth (2022). On the depth of earthquakes in the Delaware basin: A case study along the Reeves–Pecos county line, *Seism. Rec.* **2,** no. 1, 29–37.

Skoumal, R. J., and D. T. Trugman (2021). The proliferation of induced seismicity in the Permian basin, Texas, *J. Geophys. Res.: Solid Earth* **126,** e2021JB021921, doi: 10.1029/2021JB021921.

Skoumal, R. J., A. J. Barbour, M. R. Brudzinski, T. Langenkamp, and J. O. Kaven (2020). Induced seismicity in the Delaware basin, Texas, *J. Geophys. Res.: Solid Earth* **125,** e2019JB018558, doi: 10.1029/2019JB018558.

Skoumal, R. J., J. O. Kaven, A. J. Barbour, C. Wicks, M. R. Brudzinski, E. S. Cochran, and J. L. Rubinstein (2021). The induced M_w 5.0 March 2020 West Texas seismic sequence, *J. Geophys. Res.: Solid Earth* **126,** e2020JB020693, doi: 10.1029/2020JB020693.

Smye, K., D. A. Banerji, R. Eastwood, G. McDaid, and P. Hennings (2021). Lithology and reservoir properties of the Delaware mountain group of the Delaware basin and implications for saltwater disposal and induced seismicity, *J. Sediment. Res.* **91,** no. 11, 1113–1132.

Smye, K. M., J. Ge, A. Calle, A. Morris, E. A. Horne, R. L. Eastwood, R. Darvari, J. P. Nicot, and P. Hennings (2024). Role of deep fluid injection in induced seismicity in the Delaware basin, west Texas and southeast New Mexico, *Geochem. Geophys. Geosys.* **25,** e2023GC011260, doi: 10.1029/2023GC011260.

Tan, X., and S. K. Lui (2024). Potential poroelastic triggering of the 2020 M 5.0 Mentone earthquake in the Delaware basin, Texas, by shallow injection wells, *Bull. Seismol. Soc. Am.* **114,** no. 2, 882–894.

Texas Seismological Network and Seismology Research at University of Texas at Austin (2025). TexNet high resolution earthquake catalog, doi: 10.15781/76hj-ed46.

Trugman, D. T., and P. M. Shearer (2017). Growclust: A hierarchical clustering algorithm for relative earthquake relocation, with application to the Spanish springs and Sheldon, Nevada, earthquake sequences, *Seismol. Res. Lett.* **88,** no. 2A, 379–391.

Tung, S., G. Zhai, and M. Shirzaei (2021). Potential link between 2020 Mentone, West Texas M 5 earthquake and nearby wastewater injection: Implications for aquifer mechanical properties, *Geophys. Res. Lett.* **48,** e2020GL090551, doi: 10.1029/2020GL090551.

U.S. Energy Information Administration (2024). *Drilling productivity report: Summary*, *Technical Rept.*, U.S. Energy Information Administration (EIA).

Verdecchia, A., E. S. Cochran, and R. M. Harrington (2021). Fluid-earthquake and earthquake-earthquake interactions in southern Kansas, USA, *J. Geophys. Res.: Solid Earth* **126,** e2020JB020384, doi: 10.1029/2020JB020384.

Walsh, R., and M. Zoback (2015). Oklahoma's recent earthquakes and saltwater disposal, *Sci. Adv.* **1,** doi: 10.1126/sciadv.1500195.

Watkins, T. J. M., J. P. Verdon, and G. Rodríguez-Pradilla (2023). The temporal evolution of induced seismicity sequences generated by low-pressure, long-term fluid injection, *J. Seismol.* **27,** no. 2, 243–259.

Zhai, G., M. Shirzaei, and M. Manga (2021). Widespread deep seismicity in the Delaware basin, Texas, is mainly driven by shallow wastewater injection, *Proc. Natl. Acad. Sci. Unit. States Am.* **118,** no. 20, e2102338118, doi: 10.1073/pnas.2102338118.

Manuscript received 27 August 2025
Published online 23 January 2026